Current Science
CS 5 (5), 5033-5048 (2025)
Received 18 July 2025 | **Revised 20 August** 2025 | **Accepted 22 September** 2025 | **Online Available 24 October** 2025
https://doi.org0/10.52845/CS/2025-5-5-52

Current Science

Current Science

OPEN ACCESS

ISSN(O)2795-8639

Original Article

Optimization and Effectiveness Study of Solar-Powered Intel-Ligent Water Cir-Culation and Reoxygenation Device for Urban Lakes

Min Zhang[1,2,3], Jianguo Wang[1, 2, 3, *], Fang Yang[1, 2, 3, *], Weichang Chen[1, 2, 3], Gaofeng Chen[1, 2, 3], Xu Kang[4], Xiaoting Wei[4], Xiaoping Zhu[1, 2, 3], Fang Guo[1, 2, 3]

[1]Pearl River Water Resources Research Institute, Pearl River Water Resources Commission of the Ministry of Water Resources, Guangzhou 510611, China

[2]Key Laboratory of the Pearl River Estuary Regulation and Protection of Ministry of Water Resources, Guang-zhou 510611, China

[3]Guangdong Provincial Engineering Technology Research Center for Life and Health of River & Lake, Guang-zhou 510611, China

[4]Shenzhen Shenshui Water Resources Consulting Co., Ltd., Shenzhen 518024, China

[*]Corresponding Author: Jianguo Wang; Fang Yang

Abstract:
Urban landscape and artificial lakes, key ecological infrastructure, are prone to eu-trophication and degradation due to pollution sensitivity. Existing reoxygenation technologies have high energy use, poor maintainability, and side effects. This study developed a so-lar-powered intelligent reoxygenation device with a buoy as carrier, in-tegrating above-water (main controller, motor) and underwater (impeller, flow guide, sensors) components. Via mi-cro-lifting technology, it generates horizontal and vertical circulation for exchange and reoxy-genation, with intelligent regulation via closed-loop feedback. Hydrodynamic simulations opti-mized parameters, showing maximum cir-culation at 270 mm impeller diameter (matching pipe diameter), full submersion, and 322 rpm, with tracer particles spreading over 30 m radius to form large-scale 3D circu-lation. Laboratory physical model tests validated the device's water circula-tion effect and its capacity to increase dissolved oxygen (DO) by 2.7 mg/L. Field trials de-mon-strated that under a 10 W power input, the device increases DO by 1.11-1.66 mg/L during the day and 1.05-1.29 mg/L at night. With advantages of low energy consump-tion (powered by solar energy with battery backup for continuous operation), low maintenance costs (avoiding pipeline clogging), and ecological friendliness (no signif-icant adverse impacts on aquatic eco-systems), this device provides an effective tech-nical solution for eutrophication control in urban lakes.

Keywords: solar-powered water reoxygenation device; urban lakes; eutrophication control; dissolved oxygen improvement; hydrodynamic optimization

1. Introduction

As crucial ecological infrastructure in the process of ur-banization, urban landscape lakes and artificial lakes serve as windows for urban residents to connect with nature, playing a significant role in local climate regulation, biodiversity con-servation, and the creation of water culture [1-3]. However, as typical lentic ecosystems, urban lakes exhibit distinct charac-teristics of pollution sensitivity and vulnerability: first, the in-put of non-point source pollution is complex, affected by mul-tiple factors such as leakage from municipal pipe networks and

pollutants carried by surface runoff [4-6]; second, hydro-dynamic conditions are limited, with the water exchange cycle generally exceeding 30 days (even reaching several months in ultra-shallow areas), forming "dead zones" where dissolved oxygen concentrations remain below 4 mg/L for a long time [7, 8]; third, endogenous pollution accumulates continuously, with the organic matter content in sediment exceeding the standard (>5%) [9, 10]; fourth, artificial islands and hardened revetments increase ecological load and compress the biologi-cal habitats on the bank slopes [11-13]. In summary, due to factors such as the continuous input of exogenous pollution, continuous accumulation of endogenous pollution, and insuf-ficient dissolved oxygen, water eutrophication and the degra-dation of ecosystem structure and function have always been problems plaguing the health and operation management of urban lakes.

Studies have shown that aeration reoxygenation technol-ogy is an effective restoration measure for urban lakes suffer-ing from eutrophication and degradation of ecosystem struc-ture and function. Reoxygenation technology can significantly increase dissolved oxygen (DO) content, inhibit anaerobic mi-crobial activity, and reduce the release of endogenous pollu-tants (such as nutrients and heavy metals in sediments) [14-16]. Meanwhile, by disrupting water stratification (e.g., deep-water aeration) or directly oxidizing sediments, aeration can reduce the release of nitrogen and phosphorus from sedi-ments and lower endogenous loads [16-18]. Additionally, it can stimulate the growth of specific microbial groups (e.g., Planktomycetes, denitrifying bacteria) to accelerate the re-moval of nitrogen pollutants [18, 19]. Currently, common re-oxygenation methods for urban lake waters include artificial aeration, hydraulic regulation, and ecological restoration. Ar-tificial aeration improves anoxic conditions by injecting oxy-gen into the water bottom via mechanical devices (e.g., aera-tors, oxygenation pumps) [20]. In urban lakes such as Wuhan East Lake, artificial aeration significantly increased the bottom DO concentration (from 0 mg/L to near saturation), effectively inhibiting the release of endogenous pollution from sediments [21, 22]. In Lake Jeziorak Mały, a shallow urban lake in Poland, the application of a fountain aeration system effectively sup-pressed algal blooms and improved water transparency [23]. In Canada's Wilcox Lake, where urbanization has led to dis-solved oxygen depletion and algal blooms, studies have indi-cated the need for hydraulic regulation (e.g., increasing water mixing) to alleviate hypoxia [24]. Wuhan's river-lake connec-tivity project improved the dissolved oxygen distribution in the urban river-lake network by enhancing water mobility [25]. Sun et al. (2024) confirmed that regulating hydraulic condi-tions (e.g., water level, flow velocity) significantly improved water quality in Dongping Lake, Tai'an City, Shandong Prov-ince, particularly in enhancing dissolved oxygen levels [26]. Studies have shown that the recovery of submerged plants sig-nificantly increased water dissolved oxygen in the dense sub-merged plant areas of Wuliangsuhai Lake, thereby inhibiting nitrous oxide emissions and playing a dual role in improving water quality and regulating greenhouse gas emissions [27].

However, existing urban water reoxygenation technolo-gies have limitations. For instance, artificial aeration reoxy-genation features high energy consumption and operational costs, may trigger secondary release of nutrient salts from sediment to exacerbate eutrophication, relies on empirical models for regulation with insufficient precision, and requires frequent equipment maintenance. Hydraulic regulation reox-ygenation depends on natural water mobility, with poor effec-tiveness in still or slow-flowing conditions; it may disturb sediment to cause pollutant diffusion, and excessively rapid reoxygenation is prone to inducing biological oxidative stress.

Ecological restoration reoxygenation takes effect slowly and demands long-term maintenance; plant-based reoxygenation may lead to secondary hypoxia due to decay, involves complex ecosystem construction, is vulnerable to extreme climate dis-turbances, and has limited adaptability to water bodies with high pollution loads [14, 28, 29]. In view of this, this study has developed a solar-powered intelligent water reoxygenation device, aiming to improve hydrodynamics and dissolved oxy-gen exchange in water bodies such as urban landscape pools and artificial lakes, promote the recovery of water self-purification capacity, and mitigate eutrophication in ur-ban lakes with low energy consumption.

2. Materials and Methods

2.1 Overall Architecture and Functions of the Device

2.1.1 Device Structure and Design Principle

The aquatic ecological restoration device uses a buoyant body as its carrier, divided into above-water and underwater components (Figure 1). The above-water part includes a main controller and a motor mounted on the buoyant body, while the underwater part comprises an impeller, a flow-guiding structure, and a dissolved oxygen sensor. The impeller is fixed under the buoyant body via a connecting shaft and extends into shallow water. The flow-guiding structure consists of a water distribution plate and a water pressure plate: the former is connected and secured to the buoyant body through a bracket, and the latter is fixed under the buoyant body, above the impeller. A horizontal flow-guiding space for water flow is formed between them, and their combination ensures the micro-lifting effect of the water body, maximizing the circulating water volume under a given motor power.

When the impeller rotates, it drives the water to generate horizontal flow and creates local negative pressure nearby, which lifts deep water at the bottom of the pipe to the upper layer under atmospheric pressure. Meanwhile, deep water around the pipe bottom is supplemented into the pipe through the water inlet to form vertical flow. Shallow water enters the water distribution plate under the impeller's action, and under the combined effect of the water distribution plate and water pressure plate, both horizontal and vertical water circulation are established. This dual circulation promotes the exchange between shallow and deep water, increasing dissolved oxygen levels-especially in deep water. Characterized by micro-lifting technology for layered water exchange, the device features low power consumption and can be powered by solar energy combined with lithium batteries.

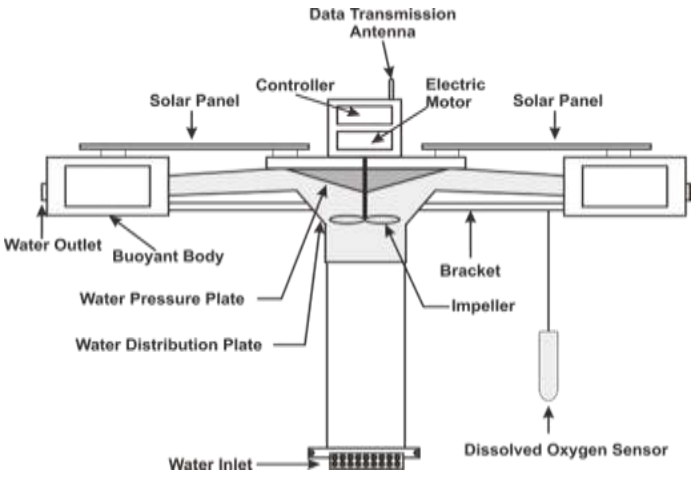

Figure 1. Schematic diagram of solar-powered intelligent water circulation and reoxygenation device.

2.1.2 Overall Functions and Control Strategy of the Device

The solar-powered intelligent aquatic ecological restoration system utilizes solar energy as supplementary power to achieve energy self-sufficiency without the need for external power supply. Based on water micro-lifting technology, the system adopts an optimally designed structure derived from hydrodynamic simulation analysis. Through the impeller-driven water flow and flow-guiding devices, it breaks water stratification and creates vertical exchange and horizontal circulation of water bodies, particularly enhancing vertical exchange between bottom and surface waters to reoxygenate the bottom layer. Meanwhile, the circulating water flow also helps prevent and control algal blooms.

For the overall control of the device, a closed-loop feedback control strategy is adopted. Equipped with dissolved oxygen sensors and depth sensors, the device monitors real-time parameters including dissolved oxygen levels, water depth, and equipment power. It can dynamically adjust restoration strategies according to changes in monitored indicators, conduct full-process monitoring of the restoration process for polluted water bodies, and ensure restoration effectiveness while maintaining low energy consumption.

2.2 Hydrodynamic Simulation

2.2.1 Hydrodynamic Mathematical Model

Using a three-dimensional hydrodynamic model, the effects of factors such as impeller diameter, impeller rotation speed, draft tube diameter, draft tube length, and impeller immersion depth on the flow velocity inside the draft tube are simulated. This model analyzes the vertical flow characteristics, planar flow characteristics, and the three-dimensional process of the entire water circulation during the device's water circulation, thereby realizing the optimal design of the device. In the three-dimensional model, the motion equation is the Navier-Stokes (N-S) equation, with the RNG k-ε turbulence model incorporated into it. The expressions of the continuity equation and the motion equation in the model are as follows:

$$\frac{\partial}{\partial x}(uA_x)+\frac{\partial}{\partial y}(vA_y)+\frac{\partial}{\partial z}(wA_z)=0,$$

$$\frac{\partial u}{\partial t}+\frac{1}{V_F}\left\{uA_x\frac{\partial u}{\partial x}+vA_y\frac{\partial u}{\partial y}+wA_z\frac{\partial u}{\partial z}\right\}=-\frac{1}{\rho}\frac{\partial p}{\partial x}+G_x+f_x$$

$$\frac{\partial v}{\partial t}+\frac{1}{V_F}\left\{uA_x\frac{\partial v}{\partial x}+vA_y\frac{\partial v}{\partial y}+wA_z\frac{\partial v}{\partial z}\right\}=-\frac{1}{\rho}\frac{\partial p}{\partial y}+G_y+f_y$$

$$\frac{\partial w}{\partial t}+\frac{1}{V_F}\left\{uA_x\frac{\partial w}{\partial x}+vA_y\frac{\partial w}{\partial y}+wA_z\frac{\partial w}{\partial z}\right\}=-\frac{1}{\rho}\frac{\partial p}{\partial z}+G_z+f_z$$

Where A_x, A_y, Az represent the flowable area integrals in the x, y and z directions, respectively; u, v and w correspond to the velocity components in the x, y, and z directions, respectively; V_F denotes the flowable volume fraction; ρ represents the fluid density; G_x, G_y and G_z denote the gravitational accelerations in the x, y and z directions, respectively; and f_x, f_y and f_z represent the viscous forces in the x, y and z directions, whose expressions are as follows:

$$\rho V_F f_x=-\left\{\frac{\partial}{\partial x}(A_x\tau_{xx})+\frac{\partial}{\partial y}(A_y\tau_{xy})+\frac{\partial}{\partial z}(A_z\tau_{xz})\right\},$$

$$\rho V_F f_y=-\left\{\frac{\partial}{\partial x}(A_x\tau_{xy})+\frac{\partial}{\partial y}(A_y\tau_{yy})+\frac{\partial}{\partial z}(A_z\tau_{yz})\right\},$$

$$\rho V\ f_z = -\left\{\frac{\partial}{\partial x}(A_x\tau_{xz}) + \frac{\partial}{\partial y}(A_y\tau_{yz}) + \frac{\partial}{\partial z}(A_z\tau_{zz})\right\},$$

Where τ represents the liquid shear stress, where the subscripts indicate the acting surface and direction of the liquid shear stress, respectively. The specific expression of τ is as follows:

$$\tau_{xx} = -2\mu\left\{\frac{\partial u}{\partial x} - \frac{1}{3}\left(\frac{\partial u}{\partial x} + \frac{\partial v}{\partial y} + \frac{\partial w}{\partial z}\right)\right\},$$
$$\tau_{yy} = -2\mu\left\{\frac{\partial v}{\partial y} - \frac{1}{3}\left(\frac{\partial u}{\partial x} + \frac{\partial v}{\partial y} + \frac{\partial w}{\partial z}\right)\right\},$$
$$\tau_{zz} = -2\mu\left\{\frac{\partial w}{\partial z} - \frac{1}{3}\left(\frac{\partial u}{\partial x} + \frac{\partial v}{\partial y} + \frac{\partial w}{\partial z}\right)\right\},$$
$$\tau_{xy} = \tau_{yx} = -\mu\left(\frac{\partial v}{\partial x} + \frac{\partial u}{\partial y}\right),$$
$$\tau_{xz} = \tau_{zx} = -\mu\left(\frac{\partial v}{\partial z} + \frac{\partial w}{\partial x}\right),$$
$$\tau_{yz} = \tau_{zy} = -\mu\left(\frac{\partial v}{\partial z} + \frac{\partial w}{\partial y}\right),$$

The RNG k-ε turbulence model is as follows:

$$\text{equation}: \frac{\partial(\rho k)}{\partial t} + \frac{\partial(\rho k u_i)}{\partial x_i} = \frac{\partial}{\partial x_j}\left[\alpha_k \mu_{eff}\frac{\partial k}{\partial x_j}\right] + G_k + \rho\varepsilon,$$
$$\text{equation}: \frac{\partial(\rho\varepsilon)}{\partial t} + \frac{\partial(\varepsilon u_i)}{\partial x_i} = \frac{\partial}{\partial x_j}\left[\alpha_\varepsilon \mu_{eff}\frac{\partial \varepsilon}{\partial x_j}\right] + \frac{C_{1\varepsilon}\varepsilon}{k}G_k - C_{2\varepsilon}\rho\frac{\varepsilon^2}{k},$$

Where ρ is the fluid density; k is the turbulent kinetic energy; u_i is the velocity tensor; ε is the turbulent kinetic energy dissipation rate; μ_{eff} is the effective viscosity; G_k is the production term of turbulent kinetic energy k; $C_{1\varepsilon}$ and $C_{2\varepsilon}$ are empirical constants; α_k and α_ε are constants with a value of 1.39; t is time; x_i and x_j are coordinate tensors.

2.2.2 Hydrodynamic Hydrodynamic Model Simulation Method

The hydrodynamic simulation of this device is mainly conducted using FLOW-3D simulation software (Version 2023R1, Flow Science, Inc., Santa Fe, NM, USA). First, a 3D model of the floating body is constructed using Auto CAD software, and the STL file obtained is imported into the model for modeling. By setting the rotation speed of the impeller to simulate real working conditions, the water flow distribution and the flow rate in the draft tube are obtained. Through 3D model tests, the overall flow situation of the water body in the water area under various working conditions can be obtained; through 2D slices, the hydraulic situation at local positions can be understood; by drawing velocity contour lines, streamline diagrams, etc., the direction and magnitude of the water flow can be clarified, which is conducive to understanding the oxygenation effect of the aquatic ecological restoration system on the water body and the exchange situation of the entire water body. Finally, through particle tracking, the influence range of the sprayed water body (particle source) can be accurately judged, and the oxygenation improvement range of the water body under various working conditions can be determined.

2.2.3 Laboratory Physical Model Device

To verify the validity of the simulation results, a small-scale physical model of the device was built in the laboratory. The laboratory device was

constructed according to the parameters shown in Figure 2. The water body is held in a transparent acrylic tank, and the draft tube is also made of transparent acrylic. To visually observe the water circulation, red PMMA particles with a density of 1.1 g/cm³ were used as tracer particles. To test the device's effect on improving the dissolved oxygen content in the water, a dissolved oxygen sensor (Shanghai LEICI JPB-607A) was installed at the bottom of the inner wall of the acrylic tank.

Parameters of the Laboratory Physical Model Device

Items	Value
Impeller Diameter	125 mm
Impeller Speed	500 rpm
Diversion Pipe Diameter	160 mm
Diversion Pipe Longth	500 mm
Water Surface Area	0.2075 m²
Water Depth	0.6 m

Figure 2. Schematic diagram and design parameters of the laboratory bench-scale device

2.3 On-Site Verification Experiment of the Device's Reoxygenation Effect

The maximum operating power of the circulation device is 100 W, with a supporting 200 A·h/12h storage battery and a 300 W solar panel. On sunny days, calculated based on an effective daily sunshine duration of 8 hours in South China and an overall charging efficiency of 80% for the solar panel, the daily chargeable electricity is 1.920 kW·h. Under the operating condition of maintaining a constant maximum power of 100 W, the maximum possible continuous working time is 5 days. During consecutive cloudy and rainy days, relying on the storage battery's power, under the same operating condition of a constant maximum power of 100 W, the maximum possible continuous working time is 1 day. In practical applications, combined with the automatic power adjustment control strategy, the device can be guaranteed to operate continuously and normally online. When the remaining power drops to the warning threshold, the device sends a low-battery alarm signal and enters the dormant standby charging state, with the motor stopping operation.

To test the water circulation and reoxygenation effect of the device, on-site debugging and experiments were conducted respectively on March 24, 2024, and October 24, 2024, at Longhu Lake of the College of Chinese Language and Culture, Jinan University in Tianhe District, Guangzhou, and the central ecological pond of the Guanlan River Basin in Shenzhen. Meanwhile, a real-time online monitoring buoy platform for water dissolved oxygen was deployed 2 meters away from the reoxygenation device, which can verify the actual reoxygenation effect of the solar-powered physical circulation reoxygenation device both at night and during the day (Figure 3).

Figure 3. On-site layout of the prototype device

3. Results and Discussion

3.1. Optimization of Device Design Parameters Based on Hydrodynamic Model Simulation

To investigate each potential influencing factor, a simulation method with only one variable changed at a time was adopted, focusing on three types of working conditions: impeller diameter, impeller immersion depth, and different rotational speed-impeller diameter ratios under the same input power. The optimization target was to maximize the flow rate inside the draft tube. As shown in the simulation results in Table 1, the larger the impeller diameter, the greater the internal circulation flow rate; the closer the impeller diameter is to the tube diameter, the more obvious the increasing trend of the flow rate. When the impeller diameter reaches 290 mm, the flow rate inside the draft tube is the highest, reaching 3.500 L/s. Salehi N et al. studied the effects of different impeller designs on flow characteristics, and clearly pointed out that the ratio of impeller diameter to container diameter (i.e., the degree to which the impeller approaches the tube diameter) significantly alters flow field distribution and mixing efficiency. When the impeller diameter increases, radial flow is enhanced, and the circulation flow rate increases accordingly [30]. Zhao Z et al. noted that under a fixed pipe diameter, the inlet flow rate is positively correlated with the impeller diameter, and the transient flow velocity peak increases significantly as the impeller diameter increases. Their study also mentioned that a larger impeller diameter results in a more uniform flow field distribution and improved circulation efficiency [31]. Wang L et al. discussed impeller structures (e.g., number of blades, diameter), indicating that increasing the number of blades reduces the flow rate, while optimizing the impeller diameter and geometric shape can improve internal flow conditions and enhance circulation efficiency [32]. These studies verify the influence of impeller diameter on circulation flow rate from different perspectives, especially that when the impeller size is close to the pipe diameter, flow field disturbance is enhanced, leading to a more significant increase in flow rate. Therefore, in design, the impeller diameter should be made close to the tube diameter.

Table 1. Model calculation results of the influence of impeller diameter on flow rate

Pipe Diameter (mm)	Pipe Length (m)	Rotational Speed (rpm)	Impeller Diameter (mm)	Impeller Immersion Depth (cm)	Flow Rate (L/s)
315	2	200	290	0 [a]	3.500

315	2	200	270	0	2.640
315	2	200	250	0	1.962
315	2	200	230	0	1.610
315	2	200	210	0	1.564
315	2	200	190	0	1.368

[a], the impeller's water entry depth being 0 indicates that the impeller is just completely submerged in water

Based on the results in Table 2, as the impeller immersion depth increases, the flow rate first rises, reaching a peak value of 4.871 L/s when fully submerged. As the immersion depth increases to 2 cm, the flow rate drops to 3.906 L/s and then stabilizes between 3.903 L/s and 3.917 L/s with further increases in depth. Bustamante et al. studied the hydrodynamic performance of different impeller types in submerged environments and pointed out that impeller type significantly influences flow patterns, energy dissipation, and power consumption, confirming the complex effects of impeller design and immersion conditions on fluid behavior [33]. When the impeller immersion depth increases, stronger vortices or flow separations (especially at the impeller edges or in narrow flow channels) may form in the flow field, increasing energy loss due to viscous dissipation [34, 35]. Research indicates that insufficient immersion depth can lead to cavitation, causing a dramatic rise in energy loss, while an appropriate increase in immersion depth can suppress cavitation and improve energy efficiency [36, 37]. However, excessive immersion depth may negate the benefits due to increased fluid resistance (resulting in a drop in energy efficiency from 75.67% to 37.21%) or uneven stirring (with extended mixing time) [34, 38]. Therefore, based on these findings, the impeller immersion depth in the present design is chosen to be fully submerged.

Table 2. Model calculation results of the effect of impeller inlet depth on flow rate

Pipe Diameter (mm)	Pipe Length (m)	Rotational Speed (rpm)	Impeller Diameter (mm)	Impeller Immersion Depth (cm)	Flow Rate (L/s)
315	2	200	290	-2	3.500
315	2	200	290	0[a]	4.871
315	2	200	290	2	3.906
315	2	200	290	4	3.903
315	2	200	290	6	3.917

[a], the impeller's water entry depth being 0 indicates that the impeller is just completely submerged in water

The simulation results in Table 3 show that when the motor output power remains constant, the combination of impeller diameter and speed with a motor speed of 322 rpm and an impeller diameter of 270 mm results in the maximum flow rate of 9.667 L/s in the diffuser. Studies have shown that there is an optimal match between impeller geometry and speed, where energy loss is minimized when the speed and impeller size are properly matched [39, 40]. Additionally, literature indicates that impeller geometry affects flow separation phenomena. In this study, the 270 mm impeller diameter and 322 rpm speed likely represent the "optimal match point" for the system, effectively controlling flow separation induced by the impeller blade angle and tip, reducing energy loss, and increasing transmission efficiency, thereby maintaining a higher flow rate [41, 42].

Table 3. Model calculation results of the effect of different speed and impeller diameter ratios on flow rate under the same motor output power

Pipe Diameter (mm)	Pipe Length (m)	Rotational Speed (rpm)	Impeller Diameter (mm)	Flow Rate (L/s)
315	2	300	290	9.084

315	2	322	270	9.667
315	2	348	250	9.386
315	2	378	230	9.149
315	2	458	190	9.223

Note: when the product of impeller diameter and speed is constant, the motor's output power remains constant.

Based on the above simulations for the three operating conditions: impeller diameter, impeller inlet depth, and different speed and impeller diameter ratios under the same input power, the optimal condition was selected with an impeller diameter of 270 mm, speed of 322 rpm, and the impeller just submerged in water. Hydrodynamic simulations were then performed to trace the diffusion and propagation range of tracer particles. The simulation results, shown in Figure 4, indicate that under this condition, the diffusion radius of the tracer particles exceeds 30 m, forming a large-scale, three-dimensional water circulation.

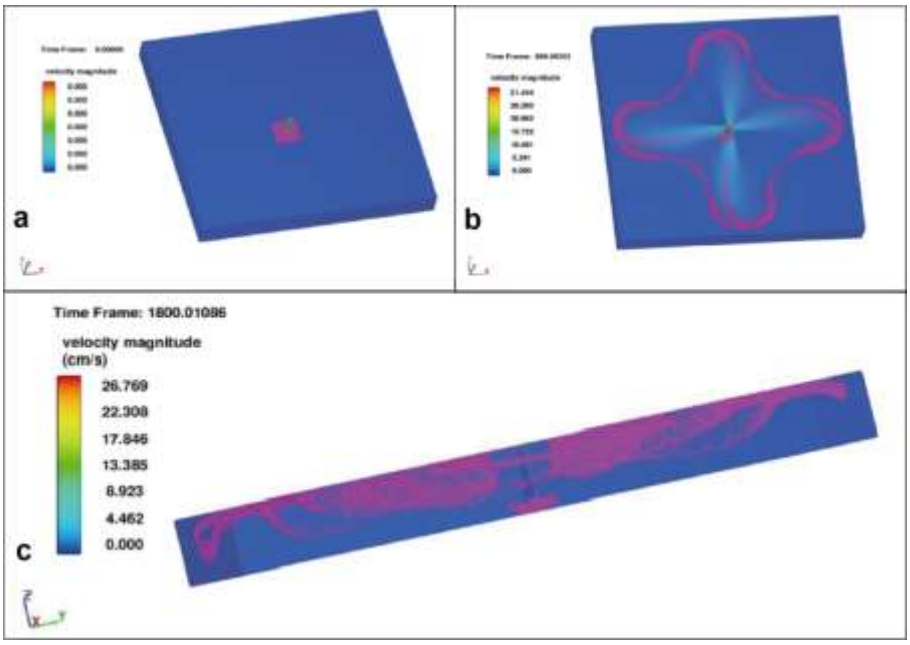

Figure 4. Tracer particle diffusion distribution of water circulation (a, initial position; b, diffusion distribution; c, longitudinal cross-section diffusion distribution)

3.2 Laboratory Physical Model Simulation Results

The laboratory physical model simulation results are shown in Figure 5. Before the motor is activated, the tracer particles are uniformly distributed at the bottom of the water. When the water circulation device is turned on, the tracer particles are gradually lifted into the diffuser tube. Once the particles reach the water surface, they are carried by the lateral flow near the surface, leaving the diffuser tube and continuing to flow along the surface. Eventually, due to gravity, they fall back to the bottom, forming a circulation. The experiment demonstrates that the water circulation generated by the laboratory physical model closely matches the simulation results. The monitored dissolved oxygen variation curve is shown below. Prior to the device startup, the dissolved oxygen level was 5.1 mg/L. After stabilization, it maintained around 7.8 mg/L, and after the device was stopped, it decreased back to 5.3 mg/L, confirming the oxygenation effect of the device at the laboratory scale.

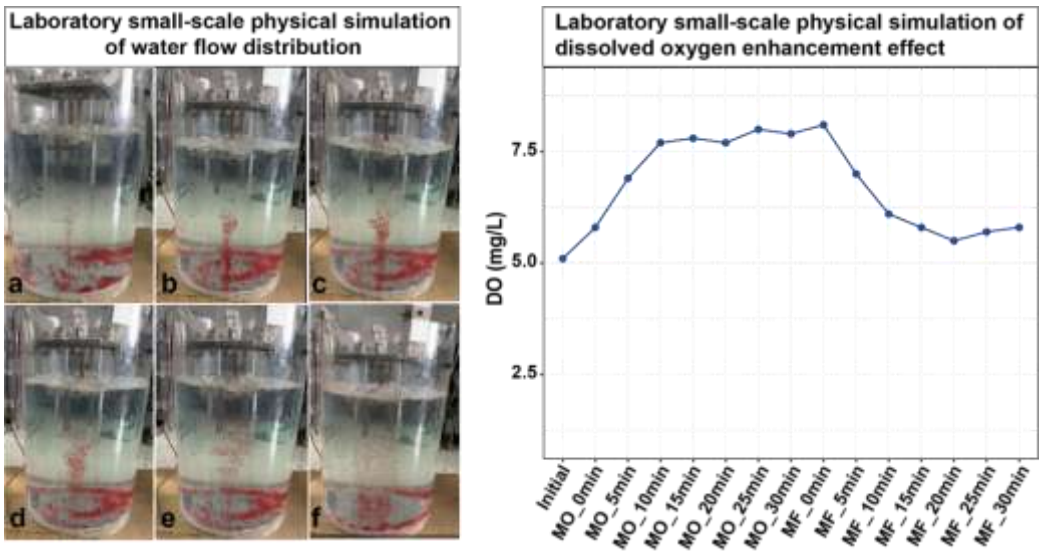

Figure 5. Laboratory physical model water flow distribution and dissolved oxygen enhancement effect (to, motor on; tf, motor off)

3.3 Field Application Effect of the Solar-Powered Water Circulation Oxygenation Prototype System

The field layout and oxygenation effect of the solar-powered water circulation oxygenation prototype system are shown in Figure 6. The prototype at Jinan University Longhu was tested for daytime oxygenation effectiveness between 15:00 and 18:20. Before the device was turned on, the average dissolved oxygen (DO) level was 5.86 mg/L. After the device was started and stabilized at a 10 W output power, the DO increased to 6.46–7.27 mg/L, with an average of 6.97 mg/L. After the system was shut down, the DO gradually decreased, finally returning to a level of 5.18 mg/L. For the nighttime oxygenation test conducted between 00:00 and 02:25, the average DO before the device was turned on was 3.40 mg/L. After stabilizing at 10 W output power, the DO increased to 4.20–4.64 mg/L, with an average of 4.55 mg/L. After turning off the device, the DO gradually dropped back to 3.13 mg/L.

The prototype at Guanlan River Basin Central Park was also tested for daytime oxygenation effectiveness between 15:00 and 18:20. The average DO before the device was turned on was 5.16 mg/L. After the motor was started and stabilized at a 10 W output power, the DO increased to 5.60–7.12 mg/L, with an average of 6.82 mg/L. After the system was shut down, the DO gradually decreased back to 5.25 mg/L. For the nighttime oxygenation test conducted between 00:00 and 02:25, the average DO before the device was turned on was 3.16 mg/L. After the device was started and stabilized at a 10 W output power, the DO increased to 3.84–4.62 mg/L, with an average of 4.45 mg/L. After turning off the device, the DO gradually dropped back to 3.28 mg/L.

The combined oxygenation effects of both prototypes during different periods indicate that this device can significantly increase the dissolved oxygen (DO) content in urban lake waters. Studies have shown that traditional aeration devices (e.g., paddle-wheel or diffused aerators) suffer from high energy consumption and maintenance costs [43, 44]. Paddle-wheel aerators typically operate within a power range of 100-200 W, while diffused aerators generally have power ratings in the kW range. Research indicates that traditional aeration technologies account for 35%-51% of the total energy consumption in wastewater treatment, leading to annual energy consumption of 500-750 million kWh [45]. In contrast, this device requires only 10 W of power to achieve a significant increase in DO levels in urban lake waters (approximately 1.11-1.66 mg/L during the day and 1.05-1.29 mg/L at night), aligning with the trend of low-energy consumption design. Furthermore, diffused aeration systems (e.g., micropore membrane aerators) often require frequent maintenance to address scaling and material aging issues, with maintenance costs increasing over time. Performance degradation varies significantly for different materials (e.g., silicone, polyurethane) under different operating conditions [46, 47]. Xiao et al (2020) found that nano-aeration technology

can enhance oxygen transfer efficiency by 1.5 times compared to traditional aeration methods [48]. However, nano-bubble aeration systems also face clogging issues due to scaling or material aging in micropore tubing. The design of this solar-powered water circulation oxygenation device avoids such clogging problems and requires low maintenance costs. Low-intensity electromagnetic field (EMF) oxygenation technology is a novel method that uses low-intensity electromagnetic radiation to promote oxygen dissolution and transfer in water. Its core mechanism involves the influence of the electromagnetic field on water molecules, dissolved oxygen, and the water interface, enhancing oxygen solubility and transfer efficiency in the water [49-51]. However, studies have shown that the low-frequency electromagnetic fields applied to water could have adverse effects on microorganisms and benthic organisms [52, 53]. Compared to this technology, the proposed device is more ecologically friendly and does not have significant negative impacts on aquatic ecosystems.

It is also worth noting that the increase in dissolved oxygen (DO) during the day (1.11–1.66 mg/L) is slightly higher than at night (1.05–1.29 mg/L), which may be related to the temperature difference between day and night and the changes in oxygen solubility caused by photosynthesis [54-56]. Although daytime warming promotes oxygen production through photosynthesis, high temperatures simultaneously suppress the physical dissolution of oxygen. At night, the temperature drop may alleviate this limitation, but the lack of photosynthesis compensation results in a weaker net oxygenation effect. Additionally, studies have pointed out that the diurnal dynamics of dissolved organic matter (DOM) in urban lakes affect microbial respiration and oxygen consumption. During the day, photodegradation of DOM reduces oxygen-consuming substrates, while at night, microbial decomposition of DOM intensifies oxygen consumption [57].

Overall, the solar-powered water circulation oxygenation device developed in this study shows clear advantages over traditional mechanical aeration, diffused aeration, and low-frequency electromagnetic field oxygenation technologies in terms of energy consumption, maintenance costs, and ecological friendliness. This highlights the synergistic effect of green energy technologies and fluid dynamics.

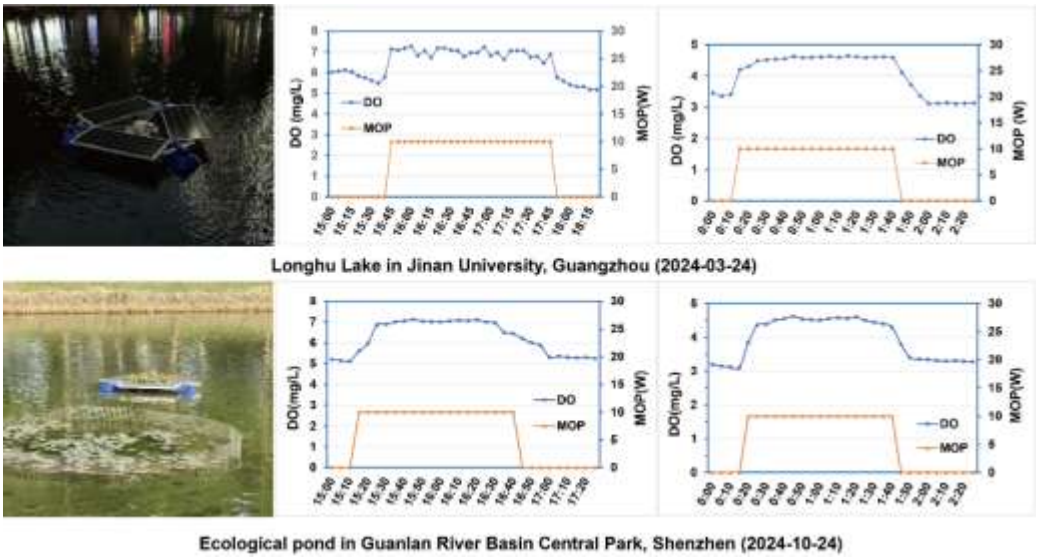

Figure 6. Prototype operation site and dissolved oxygen enhancement curve

4. Conclusions

This study addresses the issues of eutrophication and ecological degradation in urban landscape lakes and artificial lakes. The developed solar-powered intelligent water oxygenation device, through optimization and testing, leads to the following conclusions: Hydrodynamic simulations show that when the impeller diameter ap-proaches the pipe diameter and the water inlet depth is fully submerged, the circula-tion flow reaches its maximum. Under constant motor output power, the combination of different impeller diameters and speeds has minimal effect on the flow rate. There-

fore, the design must consider the balance between flow rate, equipment cost, and power consumption. The laboratory physical model validated the water circulation ef-fect of the device, which can increase dissolved oxygen by 2.7 mg/L. Field tests showed that at 10 W power, the device can increase dissolved oxygen by 1.11–1.66 mg/L during the day and 1.05–1.29 mg/L at night. Additionally, the tracer particle diffusion radius exceeds 30 m, forming a large-scale, three-dimensional water circulation. The device uses solar energy, ensuring low energy consumption. The solar panels and batteries can support continuous operation, while the design avoids pipeline clogging issues, reduc-es maintenance costs, and has no significant negative impact on the aquatic ecosystem. It is ecologically friendly and provides an effective technological solution for manag-ing eutrophication in urban lakes.

Acknowledgments:

This paper was supported from Shenzhen 2022 Special Project for Sustainable Devel-opment (NO. SP 2022N010), Guangzhou Water Affairs Science and Technology Project (NO. HCJC-2024-030), Water conservancy standard management (NO. 102126222060080009026), Major science and technology projects of the Ministry of Water Resources (No. SKS-2022064) and National Natural Science Foundation of China (NSFC42007293).

Conflict of Interest

The authors declare that they have no known competing financial interests or personal relationships that could have appeared to influence the work reported in this paper.

References

1. Hill, M.J., Biggs, J., Thornhill, I., et al. Urban ponds as an aquatic biodiversity resource in modified landscapes. *Global Change Biol*. 2017,23(3),986-999. https://doi.org/10.11 11/gcb.13401.
2. Jacobs, C., Klok, L., Bruse, M., et al. Are urban water bodies really cooling? *Urban Clim.* 2020,32,100607. https://doi.org/10.10 16/j.uclim.2020.100607.
3. Zhang, R., Taylor K. Cultural landscape meanings. The case of West Lake, Hangzhou, China. *Landscape Res.* 2020, 45(2), 164-178. https://doi.org/10.1080/01426397.2019.1589 438.
4. Andersson, M., Eggen, O.A. Urban contamination sources reflected in inorganic pollution in urban lake deposits, Bergen, Norway. *Environ. Sci.: Processes Impacts* 2015,17(4),854-867. https://doi.org/10.1039/ C4EM00614C.
5. Tenagne, A.W. The impact of urban storm water runoff and domestic waste effluent on water quality of Lake Tana and local groundwater near the city of Bahir Dar, Ethiopia. Ethiopia, Cornell University, 2009; pp.1-2.
6. Yang, Q., Shen, C., Li, Z. Bibliometric analysis of global performance and trends of research on combined sewer overflows (CSOs) from 1990 to 2022. *Water Sci. Technol.* 2024, 89(6), 1554-1569. https://doi. org/10.2166/wst.2024.074.
7. Mi, C., Rinke, K., Shatwell, T. Optimizing selective withdrawal strategies to mitigate hypoxia under water-level reduction in Germany's largest drinking water reservoir. *J. Environ. Sci.* 2024, 146, 127-139. https://doi. org/10.1016/j.jes.2023.06.025.
8. MK, V.S., Joseph, S., PS, A., et al. A coastal Ramsar site on transition to hypoxia and tracking pollution sources: a case study of south-west coast of India. *Environ. Monit. Assess.* 2023,195,45. https://doi.org/10.1007 /s10661-022-10602-x.
9. Hou, Y., Li, B., Feng, G.C., et al. Responses of bacterial communities and organic matter degradation in surface sediment to *Macrobrachium nipponense* bioturbation. *Sci. Total Environ*. 2021,759,143534. https://doi. org/10.1016/j.scitotenv.2020.143534.
10. Yang, S., Yang, Q., Song, X., et al. A novel approach to evaluate potential risk of organic enrichment in marine aquaculture farms: a

case study in Sanggou Bay. *Environ. Sci. Pollut. Res.* 2018, 25(17), 16842-16851. https://doi.org/10.1007/s11356-018-1828-2.

11. Gittman, R.K., Fodrie, F.J., Popowich, A.M., et al. Engineering away our natural defenses: an analysis of shoreline hardening in the US. *Front. Ecol. Environ.* 2015, 13(6), 301-307. https://doi.org/10.1890/150065.
12. Man, Z., Xie, C.K., Jiang, R.Y., et al. Effects of revetments on soil ecosystems in the urban river-riparian interface. *IScience* 2022, 25(11),105277. https://doi.org/10.10 16/j.isci. 2022.105277.
13. LóPEZ-SáNCHEZ A, SáNCHEZ I, HERRáEZ F, et al. Identifying keystone connectivity spots under climate change: Implications to conservation and management of riparian systems. *J. Environ. Manage.* 2024,351,119782. https://doi.org /10.1016/j.jenvman.2023.119782.
14. Wang, H.L., Zhang, W.L., Hou, X., et al. Alternative states in microbial communities during artificial aeration: Proof of incubation experiment and development of recurrent neural network models. *Water Res.* 2023, 247,120828. https://doi.org/10.1016/j. watres. 2023.120828.
15. Li, G., Jaisi, D.P., Wang, M., et al. Zeolite facilitates sequestration of heavy metals via lagged Fe (II) oxidation during sediment aeration. *J. Hazard. Mater.* 2024, 469, 133961. https://doi.org/10.1016/j.jhazmat.20 24.133961.
16. Kibuye, F.A., Zamyadi, A., Wert, E.C. A critical review on operation and performance of source water control strategies for cyanobacterial blooms: Part II-mechanical and biological control methods. *Harmful Algae* 2021, 109, 102119. https://doi.org/10. 1016/j.hal.2021.102119.
17. Wu, D., Shen, C.Q., Cheng, Y., et al. Phosphorus removal by aquatic vegetation in shallow eutrophic lakes: a laboratory study. *Environ. Sci. Pollut. Res.* 2023, 30(6), 16166-16177. https://doi.org/10.1007/s11356-022-23403-z.
18. Zhang, D., Wang, Y.Y., Yang, H.L., et al. Using intermittent moving aeration to repair hypereutrophic pond: nutrient removal efficiency and microbial diversity analysis. *Environ. Sci. Pollut. Res.* 2023, 30(16), 46 697-46710. https://doi.org/10.1007/s11356-023-25368-z.
19. Zhang, D., Yang, H.L., Lan, S.H., et al. Evolution of urban black and odorous water: The characteristics of microbial community and driving-factors. *J. Environ. Sci.* 2022, 112,94-105. https://doi.org/10.1016/j.jes.202 1.05.012.
20. Pastorok R.A., Ginn T.C., Lorenzen, M.W. Evaluation of aeration/circulation as a lake restoration technique. Environmental Research Laboratory, Office of Research and Development, US Environmental Protection Agency, Washingtom DC, USA, 1981. pp. 1-2.
21. He, S.W., Song, N., Yao, Z.B., et al. An assessment of the purification performance and resilience of sponge-based aerobic biofilm reactors for treating polluted urban surface waters. *Environ. Sci. Pollut. Res.* 2022,29(30),45919-45932. https://doi.org/ 10.1007/s11356-022-19083-4.
22. Zhou, Z.Z., Huang, T.L., Gong, W.J., et al. Field research on mixing aeration in a drinking water reservoir: Performance and microbial community structure. Int. J. *Environ. Res. Public Health* 2019, 16(21), 4221. https://doi.org/10.3390/ijerph162142 21.
23. Zębek, E., Napiórkowska-Krzebietke, A. Response of phytoplankton to protective-restoration treatments enhancing water quality in a shallow urban lake. *Environ. Monit. Assess.* 2016,188(11),623. https://doi. org/10.1007/s10661-016-5633-4.
24. Radosavljevic, J., Slowinski, S., Shafii M., et al. Salinization as a driver of eutrophication

symptoms in an urban lake (Lake Wilcox, Ontario, Canada). *Sci. Total Environ.* 2022, 846, 157336. https://doi.org/10.1016/j. scitotenv.2022.157336.

25. Wang, C.L., Xv, Y.H., Wu, Z.F., et al. Denitrification regulates spatiotemporal pattern of N_2O emission in an interconnected urban river-lake network. *Water Res.* 2024, 251,121144. https://doi.org/10.1016 /j.watres. 2024.121144.
26. Sun, R., Wei, J.L., Zhang, S.S., et al. The dynamic changes in phytoplankton and environmental factors within Dongping Lake (China) before and after the South-to-North Water Diversion Project. *Environ. Res.* 2024, 246,118138. https://doi.org/10.1016/ j.envres. 2024.118138.
27. Ni, M., Liang, X., Hou, L.J., et al. Submerged macrophytes regulate diurnal nitrous oxide emissions from a shallow eutrophic lake: A case study of Lake Wuliangsuhai in the temperate arid region of China. *Sci. Total Environ.* 2022, 811, 152451. https://doi.org/10.1016/j.scitotenv.2021.152451.
28. Meng, Q.C., Pan, Y.W., Xuan, J.L., et al. Leveraging artificial oxygenation efficacy for coastal hypoxia by taking advantage of local hydrodynamics. *Environ. Sci. Technol.* 2024, 58(49),21629-21640. https://doi.org/10.1021/ acs.est.4c07386.
29. da Silva Martins, T., Da-Silva, C.J., Shimoia, E.P., et al. Short-term reoxygenation is not enough for the recovery of soybean plants exposed to saline waterlogging. *Plant Physiol. Bioch.* 2024, 217, 109221. https://doi.org/10.1016/j.plaphy.2024.109221.
30. Salehi, N., Al-Gousous, J., Hens, B., et al. Comparative Evaluation of dissolution performance in a USP 2 setup and alternative stirrers and vessel designs: A systematic computational investigation. *Mol. Pharmaceutics* 2024, 21(5), 2406-2414. https://doi.org/10.1021/acs.molpharmaceut.3c01203.
31. Zhao, Z.J., Zhou, L., Bai, L., et al. Effects of particle diameter and inlet flow rate on gas–solid flow patterns of fluidized bed. *ACS Omega* 2023,8(7),7151-7162. https://doi.org/10.1021/acsomega.3c00118.
32. Wang, L., Yun, Z., Tang, X.Y., et al. Influence of rotor impeller structure on performance improvement of suspended axial flow blood pumps. *Int. J. Artif. Organs* 2024, 47(3), 162-172. https://doi.org/10.1177/03913988231225128.
33. Bustamante, M.C.C., Costa, C.L.L., Esperança, M.N., et al. Effect of impeller type on cellular morphology and production of clavulanic acid by *Streptomyces clavuligerus*. *Braz. J. Microbiol.* 2024, 55(2), 1167-1177. https://doi.org/10.1007/s42770-024-01306-0.
34. Li, Y., Wang, H.Y., Xi, Y.F., Sun, et al. Multi-indicator analysis of mechanical blood damage with five clinical ventricular assist devices. *Comput. Biol. Med.* 2022, 151, 106271. https://doi.org/10.1016/j.compbiomed.2022.106271.
35. Gabso, Y., Rosenfeld, M., Avrahami, I. The impact of the Impeller's hub design on the performance and blood damage in a microaxial mechanical circulatory support device–A numerical study. *Comput. Biol. Med.* 2024,179,108695. https://doi.org/10.1016/j.compbiomed.2024.108695.
36. Zhang, X., Lin, R.Y., Zhang, L.B., et al. Numerical investigation of effect of geometric parameters on performance of rotational hydrodynamic cavitation reactor. *Ultrason. Sonochem.* 2024, 103, 106790. https://doi.org/10.1016/j.ultsonch.2024.106790.
37. Walczak, J., Dzido, A., Jankowska, H., et al. Effects of various rotational speeds of hydrodynamic disintegrator on carbon, nutrient, and energy recovery from sewage sludge. *Water Res.* 2023, 243, 120365. https://doi.org/10.1016/j.watres.2023.120365.

38. Prasad, A.R., Athikesavan, M.M., Kabeel, A.E., et al. Analysis of a solar still with photovoltaic modules and electrical heater-Energy and exergy approach. *Environ. Sci. Pollut. Res.* 2022, 29(38): 57453-57465. https://doi.org/10.1007/s11356-022-19674-1.
39. Mereke, N.B., Ancha, V.R., Hendrick, P. Numerical modeling and CFD simulation of diffuser augmented dual vertical axis hydrokinetic Banki-Michell turbine. *Heliyon* 2024,10(5),e26970. https://doi.org/10.10 16/j. heliyon.2024.e26970.
40. Khan, N., Sarwar, M.K., Rashid, M., et al. Development of a sustainable portable Archimedes screw turbine for hydropower generation. *Sci. Rep.* 2025, 15(1), 5827. https://doi.org/10.1038/s41598-025-90634-8.
41. Goodin, M.S., Horvath, D.J., Kuban, B.D., et al. Computational fluid dynamics model of continuous-flow total artificial heart: right pump impeller design changes to improve biocompatibility. *ASAIO J.* 2022, 68(6), 829-838. https://doi.org/10.1097/MAT.0000000000001581.
42. Nishida, M., Nakayama, K., Sakota, D., et al. Effect of impeller geometry on lift-off characteristics and rotational attitude in a monopivot centrifugal blood pump. *Artif. organs* 2016,40(6),E89-E101. https:// doi.org/ 10.1111/aor.12697.
43. Roy, S.M., Machavaram, R., Pareek, C.M., et al. Investigating the performance of a perforated pooled circular stepped cascade aeration system for intensive aquaculture. *Heliyon* 2024,10(5),e26367. https://doi.org/ 10.1016/j.heliyon.2024.e26367.
44. Hongprasith, N., Imai, T., Painmanakul, P. Study of the liquid-film-forming apparatus as an alternative aeration system: design criteria and operating condition. *Environ. Technol.* 2017,38(12),1539-1547. https://doi.org/10. 1080/09593330.2016.1236841.
45. Zhang, S.Y., Wang, R.P., Wang, K., et al. Aeration-free in situ fenton-like reaction: specific adsorption and activation of oxygen on heterophase oxygen vacancies. *Environ. Sci. Technol.* 2024,58(4),1921-1933. https: //doi.org/10.1021/acs.est.3c08579.
46. Wang, M.Y., Mo, H.J., Liu, G.H., et al. Impact of scaling on aeration performance of fine-pore membrane diffusers based on a pilot-scale study. *Sci. Rep.* 2020, 10(1), 4902. https://doi.org/10.1038/s41598-020-61814-5.
47. Garrido-Baserba, M., Sobhani, R., Asvapathanagul, P., et al. Modelling the link amongst fine-pore diffuser fouling, oxygen transfer efficiency, and aeration energy intensity. *Water Res.* 2017, 111, 127-139. https://doi.org/10.1016/j.watres.2016.12.027.
48. Xiao, W.T., Xu, G.R. Mass transfer of nanobubble aeration and its effect on biofilm growth: Microbial activity and structural properties. *Sci. Total Environ.* 2020,703,134 976. https://doi.org/10.1016/j.scitotenv.2019. 134976.
49. Elvidge, C.K., Bihun, C.J., Davis, C., et al. No evidence for collateral effects of electromagnetic fields used to increase dissolved oxygen levels on the behavior and physiology of freshwater fishes. *Water Environ. Res.* 2022,94(6),e10747. https:// doi.org/10.1002/wer.10747.
50. Zhao, K.L., Wu, H., Zhao, X.H., et al. Study of sewage oxygenation treatment based on gas magnetization mechanism. *Water Sci. Technol.* 2022,86(10), 2545-2554. https://doi. org/10.2166/wst.2022.361.
51. Zhao, Y.Z., Yang, K.D., Su, J.Y. Effect of terahertz electromagnetic field on single-file water transport through a carbon nanotube. *Phys. Chem. Chem. Phys.* 2023, 25(37), 2565 9-25669. https://doi.org/10.1039/D3CP0307 5J.
52. Zastko, L., Makinistian, L., Tvarožná, A., et al. Intermittent ELF-MF induce an amplitude-window effect on umbilical cord blood lymphocytes. *Int. J. Mol. Sci.* 2022, 23 (22),14391. https://doi.org/10.3390/ijms2322

14391.

53. Jakubowska, M., Urban-Malinga, B., Otremba, Z., et al. Effect of low frequency electromagnetic field on the behavior and bioenergetics of the polychaete *Hediste diversicolor*. *Mar. Environ. Res.* 2019, 150, 104766. https://doi.org/10.1016/j.marenvres.2019.104766.
54. Jane, S.F., Hansen, G.J., Kraemer, B.M., et al. Widespread deoxygenation of temperate lakes. *Nature* 2021, 594(7861), 66-70. https://doi.org/10.1038/s41586-021-03550-y.
55. Zhang, F., Shi, X.H., Zhao, S.N., et al. Hypoxia cycle in shallow lakes during winter (ice-covered to melting period): Stable and decay, hypoxia, and recovery phases. *Sci. Total Environ.* 2024, 954, 176625. https://doi.org/10.1016/j.scitotenv.2024.176625.
56. Zhang, Y.B., Shi, K., Woolway, R.I., et al. Climate warming and heatwaves accelerate global lake deoxygenation. *Sci. Adv.* 2025, 11(12),eadt5369. https://doi.org/10.1126/sciadv.adt536.
57. Wang, Y., Ma, B.J., Xu, Y.J., et al. Eutrophication and dissolved organic matter exacerbate the diel discrepancy of CO2 emissions in China's largest urban lake. Environ. Sci. Technol. 2024, 58(47), 20968-20978. https://doi.org/10.1021/acs.est.4c06244.